First-Principles Anharmonic Infrared and Raman Vibrational Spectra of Materials: Fermi Resonance in Dry Ice

Published version:

DOI:10.1021/acs.jpclett.3c03372

First-Principles Anharmonic IR and Raman Vibrational Spectra of Materials: Fermi Resonance in Dry Ice

Davide Mitoli,[1] Jefferson Maul,[1] and Alessandro Erba[1, *]
[1] *Dipartimento di Chimica, Università di Torino, via Giuria 5, 10125 Torino, Italy*

(Dated: April 22, 2025)

We introduce a computational tool for the quantum-mechanical simulation of anharmonic infrared and Raman vibrational spectra of materials. The approach, implemented in the CRYSTAL software, stems from a Taylor's expansion of the potential energy surface (PES) in the basis of normal modes up to cubic and quartic terms. The PES can be sampled with four different numerical schemes at the level of density functional theory (DFT), with local, generalized-gradient, and hybrid density functional approximations. Anharmonic states are obtained by solving Shrödinger's nuclear equation with either the vibrational self-consistent field (VSCF) or vibrational configuration interaction (VCI) methods. Nuclear quantum effects (NQEs) are thus fully accounted for. Infrared intensities are computed numerically through a Berry phase approach or analytically through a coupled-perturbed (CP) approach. Raman intensities are computed analytically via the CP approach. A variety of anharmonic features of vibrational spectra of materials can be simulated, including band shifts, combination bands, overtones, resonances (first-order Fermi, second-order Darling-Dennison), and hot bands. We showcase the effectiveness of the approach on the description of a first-order Fermi resonance (FR) in CO_2 dry ice: a challenging test-case given that the FR occurs in the Raman spectrum, requires NQEs, and involves two- and three-mode couplings. Fundamental mechanistic differences with respect to the well-known FR in molecular CO_2 are addressed. This application represents the first quantum-mechanical, periodic, description of FR in dry ice.

Keywords:

Infrared (IR) and Raman spectroscopies are among the most widely used characterization techniques for structure and dynamics in materials and surface science.[1–3] The corresponding spectra can be complex and it is nowadays common practice to perform quantum-mechanical simulations (usually with density functional theory, DFT) to assist in their interpretation.[4–6] In this respect, one most often resorts to the so-called "double-harmonic" (mechanical and electrical) approximation, DHA, which finds a robust implementation in most solid-state electronic structure program packages.

Vibrational spectra can exhibit a variety of anharmonic features, such as band shifts, combination bands, overtones, resonances (first-order Fermi, second-order Darling-Dennison), and hot bands. While anharmonic band shifts can be partially corrected for via different scaling strategies still at the DHA level,[7–11] the other features above require explicit anharmonic treatment (i.e. the calculation of anharmonic energy levels and wave-functions, as well as of transition matrix elements of the dipole moment and polarizability tensors between initial and final anharmonic states).[12,13] In particular, an effective description of resonances requires the explicit account of phonon-phonon couplings beyond a mean-field approach,[14] and of nuclear quantum effects (i.e. beyond a classical description of nuclear motions, as in Born-Oppenheimer *ab initio* molecular dynamics, AIMD, for instance, where nuclei move according to Newton's equation of motion).[15,16] While several methods to go beyond the DHA have been devised in a molecular context, this is largely not yet the case for periodic systems, particularly so when phonon-phonon coupling needs to be treated beyond a mean-field approach.

In this Letter, we report on recent advances in the simulation of fully anharmonic IR and Raman spectra of materials via the vibrational configuration interaction (VCI) method. A module has been implemented in the CRYSTAL program for DFT condensed matter simulations.[17–23] The effectiveness of the approach is discussed on the description of a first-order Fermi resonance (FR) in CO_2 dry ice. Fundamental mechanistic differences with respect to the well-known FR in molecular CO_2 are addressed.

In the VCI method, the wave-function of each vibrational state s is written as a linear combination of M-mode wave-functions:

$$\Psi_s(\mathbf{Q}) = \sum_{n=1}^{N_{\rm conf}} A_{n,s}\Phi^{\mathbf{n}}(\mathbf{Q}) \; , \tag{1}$$

where $\mathbf{Q}$ are mass-weighted normal coordinates, and the sum runs over $N_{\rm conf}$ vibrational configuration functions $\Phi^{\mathbf{n}}(\mathbf{Q})$ in turn expressed as Hartree products of one-mode functions ϕ (modals): $\Phi^{\mathbf{n}}(\mathbf{Q}) = \prod_{i=1}^{M} \phi_i^{n_i}(Q_i)$, with $\mathbf{n} = (n_1, n_2, \cdots, n_i, \cdots, n_M)$ being a vibrational configuration vector of the quantum numbers of the modals. In our implementation,[18] the modals can either be the eigenfunctions of the harmonic oscillator $\phi_i^{n_i} = \psi_i^{n_i}$ (VCI@HO) or the solutions of a previous vibrational self-consistent field (VSCF) calculation for a reference configuration (VCI@VSCF): $\phi_i^{n_i} = \sum_{\mu=1}^{N_{\rm lev}} C_{\mu,n_i}\psi_i^{\mu}$ (i.e. linear combinations of HO eigenfunctions). For each vibrational state s, the corresponding wave-function and energy are obtained by solving Schrödinger's nuclear equation $\hat{H}\Psi_s = E_s\Psi_s$, where the Hamiltonian reads $\hat{H} = \sum_{i=1}^{M}\hat{T}_i + \hat{V}$, with $T_i = -1/2(\partial^2/\partial Q_i^2)$ being the one-mode kinetic energy operator, and where we expand the potential energy surface (PES) in a Taylor series up to fourth order (namely, a 4T representation of the potential):

$$\begin{aligned} V(\mathbf{Q}) \;&\simeq\; \frac{1}{2}\sum_{i=1}^{M}\omega_i^2 Q_i^2 + \frac{1}{3!}\sum_{i,j,k=1}^{M}\eta_{ijk}Q_iQ_jQ_k + \\ &+\; \frac{1}{4!}\sum_{i,j,k,l=1}^{M}\eta_{ijkl}Q_iQ_jQ_kQ_l \;, \end{aligned} \tag{2}$$

where ω_i are harmonic frequencies, and where η_{ijk} and η_{ijkl} are cubic and quartic force constants (i.e. third- and fourth-order energy derivatives with respect to normal coordinates), respectively. Within a 4T representation, the PES can be further truncated by considering only those force constants involving a maximum of n distinct modes (namely, a nM representation). In this respect, a popular representation of the PES in a molecular context is the 2M4T one, which includes all two-mode couplings up to fourth-order. Three-mode couplings play a key role in the description of the FR in dry ice, at variance with that of the gas-phase CO_2 molecule, thus requiring a 3M4T PES. We have implemented four different numerical algorithms to compute a 2M4T PES and two different algorithms to compute a 3M4T PES.[17,20]

The VCI method reduces to the construction of the Hamiltonian matrix $\mathbf{H}$ (of size $N_{\rm conf} \times N_{\rm conf}$) in the basis of configuration functions $\Phi^{\mathbf{n}}$ (i.e. with matrix elements $H_{nm} = \langle \mathbf{n}|\hat{H}|\mathbf{m}\rangle$), followed by its diagonalization: $\mathbf{HA} = \mathbf{AE}$, where $\mathbf{A}$ is the matrix containing, column-wise, the coefficients $A_{n,s}$ of the eigenstates of Eq. (1), and $\mathbf{E}$ is the diagonal matrix with the corresponding eigenvalues E_s. The VCI expansion in Eq. (1) can be truncated according to several strategies by limiting the number of excitation quanta and number of modes simultaneously excited.[18] This results in a reduction of $N_{\rm conf}$ and thus of the size of the VCI matrix.

The IR intensity associated to a transition between an initial state Ψ_i and a final state Ψ_f involves transition matrix elements of the dipole moment $\boldsymbol{\mu}$ as follows:

$$I^{\rm IR}_{i\rightarrow f} \propto \sum_{a=x,y,z} \langle i|\hat{\mu}_a|f\rangle^2 \;, \tag{3}$$

where each Cartesian component of the dipole moment operator can be expanded in a Taylor series in terms of normal coordinates:

$$\mu_a \simeq \mu_a|_{\rm eq} + \sum_{k=1}^{M}\left(\frac{\partial \mu_a}{\partial Q_k}\right)_{\rm eq} Q_k + \sum_{k,l=1}^{M}\left(\frac{\partial^2 \mu_a}{\partial Q_k Q_l}\right)_{\rm eq} Q_kQ_l + \cdots$$

Here, $\boldsymbol{\mu}|_{\rm eq}$ is the dipole moment at the equilibrium nuclear configuration and the derivatives are also evaluated at the equilibrium configuration. At present, we neglect the so-called electrical anharmonicity and thus truncate the above expansion at first order, so that Eq. (3) becomes:

$$I^{\rm IR}_{i\rightarrow f} \propto \sum_{a=x,y,z}\sum_{k=1}^{M}\left(\frac{\partial \mu_a}{\partial Q_k}\right)^2_{\rm eq} \langle i|\hat{Q}_k|f\rangle^2 \;, \tag{4}$$

where the coefficients $(\frac{\partial \mu_a}{\partial Q_k})_{\rm eq}$ are the elements of the Born tensor that we compute either numerically through a Berry phase approach or analytically through a coupled-perturbed (CP) approach,[24,25] and where the integral can be worked out as follows in a VCI@VSCF framework:

$$\begin{aligned} \langle i|\hat{Q}_k|f\rangle \;&=\; \sum_{n=1}^{N_{\rm conf}}\sum_{m=1}^{N_{\rm conf}} A_{n,i}A_{m,f}\sum_{\mu=1}^{N_{\rm lev}}\sum_{\nu=1}^{N_{\rm lev}} C_{\mu,n_k}C_{\nu,m_k}\langle\mu|\hat{Q}_k|\nu\rangle \prod_{l\neq k=1}^{M}\delta_{n_l,m_l} \\ &=\; \sum_{n=1}^{N_{\rm conf}}\sum_{m=1}^{N_{\rm conf}} A_{n,i}A_{m,f}\sum_{\mu=1}^{N_{\rm lev}-1}\langle\mu|\hat{Q}_k|\mu+1\rangle\left[C_{\mu,n_k}C_{\mu+1,m_k} + C_{\mu+1,n_k}C_{\mu,m_k}\right]\prod_{l\neq k=1}^{M}\delta_{n_l,m_l} \\ &=\; \sum_{n=1}^{N_{\rm conf}}\sum_{m=1}^{N_{\rm conf}} A_{n,i}A_{m,f}\sum_{\mu=1}^{N_{\rm lev}-1}\sqrt{\frac{\mu+1}{2\omega_k}}\left[C_{\mu,n_k}C_{\mu+1,m_k} + C_{\mu+1,n_k}C_{\mu,m_k}\right]\prod_{l\neq k=1}^{M}\delta_{n_l,m_l} \;, \end{aligned} \tag{5}$$

where in the second and third equality we have exploited the usual properties of one-mode integrals $\langle\mu|\hat{Q}_k|\nu\rangle$.

The Raman activity associated to a transition $\Psi_i \rightarrow \Psi_f$ involves transition matrix elements of the polarizability tensor $\boldsymbol{\alpha}$ (with Cartesian components α_{ab}): $\langle i|\hat{\alpha}_{ab}|f\rangle$. As we currently neglect electrical anharmonicity, each Cartesian component of the polarizability tensor can be expressed as:

$$\alpha_{ab} \simeq \alpha_{ab}|_{\rm eq} + \sum_{k=1}^{M}\left(\frac{\partial \alpha_{ab}}{\partial Q_k}\right)_{\rm eq} Q_k \;, \tag{6}$$

where the coefficients $(\frac{\partial \alpha_{ab}}{\partial Q_k})_{\rm eq}$ are the elements of the Raman tensor that we compute analytically through a coupled-perturbed (CP) approach.[26] For solid CO_2, the neglected second-derivatives of the polarizability are about 1/20 of the first-derivatives.[27,28] Each integral $\langle i|\hat{\alpha}_{ab}|f\rangle$ (hereafter described by the shorthand notation P_{ab}) thus reduces to:

$$\langle i|\hat{\alpha}_{ab}|f\rangle \equiv P_{ab} = \sum_{k=1}^{M} \left(\frac{\partial \alpha_{ab}}{\partial Q_k}\right)_{\rm eq} \langle i|\hat{Q}_k|f\rangle \; , \qquad (7)$$

where the integral $\langle i|\hat{Q}_k|f\rangle$ has already been worked out in Eq. (5) in a VCI@VSCF framework. According to Plazeck's equation,[29] the total Raman activity can be decomposed into a perpendicular and parallel component as:

$$I^{\rm Raman}_{i\rightarrow f} = I^{\rm Raman}_{\perp,i\rightarrow f} + I^{\rm Raman}_{\parallel,i\rightarrow f} \; , \qquad (8)$$

with

$$I^{\rm Raman}_{\perp,i\rightarrow f} \propto I_1 + \frac{4}{45} I_2 \qquad \text{and} \qquad I^{\rm Raman}_{\parallel,i\rightarrow f} \propto \frac{3}{45} I_2 \; , \quad (9)$$

where I_1 and I_2 are related to individual Cartesian components of the polarizability tensor as outlined below:

$$I_1 = \frac{1}{9}\Big(\sum_{a=x,y,z} P_{aa} \Big)^2 \; ; \qquad (10)$$

$$I_2 = \frac{1}{2}\Bigg[\left(P_{xx} - P_{yy}\right)^2 + \left(P_{yy} - P_{zz}\right)^2 + \left(P_{zz} - P_{xx}\right)^2 + 6\left(P_{xy}^2 + P_{xz}^2 + P_{yz}^2\right)^2 \Bigg] \; . \quad (11)$$

First-order (Fermi) resonances occur through rather different mechanisms in isolated molecules and in crystals.[27,28,30,31] Here, we consider the FR emerging in the Raman spectrum of the CO_2 molecule and corresponding molecular crystal (i.e. dry ice). In the molecule, the FR takes place because of the accidental quasi-degeneracy of two states (fundamental excitation of the symmetric stretching s and first-overtone of the bending b) that are coupled by a cubic anharmonic interatomic force constant $\eta_{sbb} \neq 0$.[32] Thus, it is an intrinsically two-phonon process (let us stress that all three-phonon interatomic force constants are zero in the molecule), as schematically depicted in the top of Figure 1 E). As a result, a single harmonic peak is split into two in the Raman spectrum, at frequencies Ω_- and Ω_+ (the so-called Fermi dyad, with splitting amplitude $\delta = \Omega_+ - \Omega_- = 103$ cm^{-1}), reflective of two states with hybrid $s + 2b$ character, with a redistribution of intensity between the two (with an intensity ratio I_+/I_- of 1.5). See Figure 1 A) for the experimental Raman spectrum of the CO_2 molecule.[33]

The Raman spectrum in the FR region of the solid is qualitatively different, with two sharp peaks Ω_- and Ω_+ (separated by δ = 108-111 cm^{-1}, with an intensity ratio I_+/I_- of 2.15-2.5) accompanied by a broad (about 50 cm^{-1} wide), almost featureless, band between them with an integrated intensity of about 10% of I_+.[30,34–38] See Figure 1 A) for the experimental Raman spectrum of the CO_2 crystal, compared to that of the molecule. The origin of these specific features must be traced back to the periodic structure of the crystal:[27,28,39] i) the presence of multiple (four in dry ice) molecules per cell generates multiple phonon branches for symmetric stretching (one of A_g and one of F_g symmetry) and bending (one of E_u and two of F_u symmetry); ii) each phonon branch is dispersed because of intermolecular interactions, with associated frequencies changing with wavevector $\mathbf{k}$. The central band in the FR spectrum of dry ice is understood as due to the so-called "two-phonon continuum" of bending modes, that is to the manifold of states of $b(\mathbf{k}) + b'(-\mathbf{k})$ character (with zero total wavevector). Note that such manifold comprises both single-mode states (i.e. first-overtones at $\mathbf{k} = \mathbf{0}$ and with branch indices $b' = b$) and two-mode states (if $\mathbf{k} \neq \mathbf{0}$ or $b' \neq b$). The two-phonon bending manifold in turn couples to fundamental excitations of symmetric stretching modes at $\mathbf{k} = \mathbf{0}$ (of either A_g or F_g symmetry) to produce the two sharp peaks, whose overall character is thus of $s(\mathbf{0}) + b(\mathbf{k}) + b'(-\mathbf{k})$ type – see the bottom of Figure 1 E) for a schematic representation of such a three-phonon process. Therefore, depending on whether there is just one bending mode (in a first-overtone) or two singly-excited bending modes involved, the states contributing to the Fermi dyad in the solid can be two- or three-phonon ones, coupled by cubic anharmonic interatomic force constants $\eta_{s\mathbf{0},b\mathbf{k},b'-\mathbf{k}} \neq 0$. Both Ω_- and Ω_+ are indeed known to embody two factor group components (one of A_g and one of F_g symmetry). High-resolution, polarized, Raman measurements on single-crystal dry ice at 6 K, with an interferometer-spectrometer instrument, were able to resolve these contributions with high accuracy.[40] The left inset of Figure 1 C) shows the experimentally resolved (resolution of 0.0055 cm^{-1}) A_g and F_g contributions to Ω_-.

Attempts at the numerical modelling of the FR in solid CO_2 have basically been of two types: i) semi-empirical (i.e. parametrized by best-fit to a set of experimental features such as peak positions of Ω_- and Ω_+, their intensity ratio I_+/I_-, and the width of the "two-phonon continuum" bending band) but within the actual "periodic" theory;[27,28,41] ii) by first-principles but through a "molecular" approach where the evolution with pressure of cubic and quartic interatomic force constants of an isolated molecule[42] (i.e. with vanishing three-phonon terms) is determined via an embedded-fragment approach.[43,44] The latter approach, by neglecting three-mode couplings and the specifics of a "periodic" description of the FR allows to get reliable predictions for δ but not for the intensities, for reasons to be addressed below.

In this Letter, we present the results of first-principles calculations on the FR in solid CO_2 within a periodic approach, for the first time. Calculations are performed with a developmental version of the CRYSTAL electronic structure package.[21,46] Dry ice is modeled in the cu-

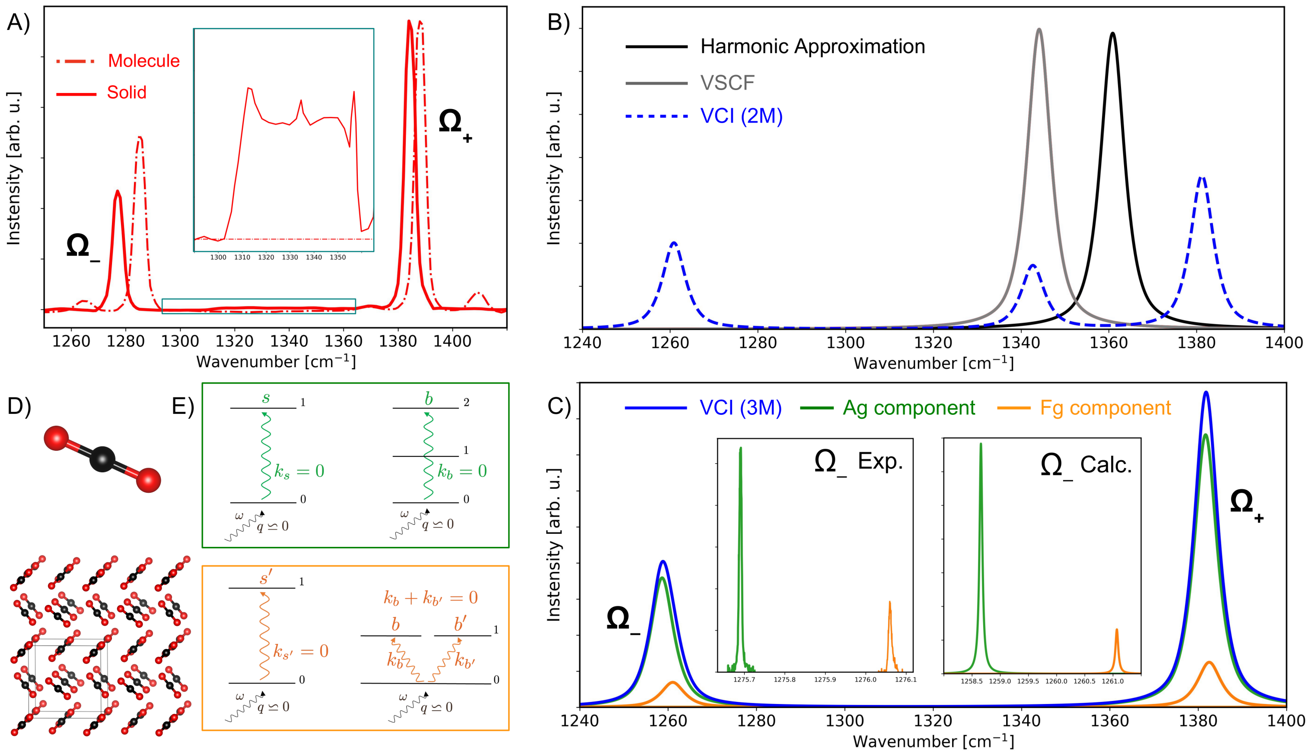

FIG. 1: Fermi resonance in the Raman spectrum of CO_2. A) Experimental Raman spectrum of the CO_2 molecule[33] (dash-dotted line) and crystal[27,33] (solid line) in the region of the Fermi dyad; the inset shows the region between the two main peaks with the "two-phonon continuum" of bending modes visible in the spectrum of the solid. B) Simulated Raman spectrum of the solid from the harmonic approximation (black solid line), the VSCF method (grey solid line) and the VCI method with a 2M4T representation of the PES (blue dashed line). C) Simulated Raman spectrum of the solid from VCI within a 3M4T representation of the PES (blue solid line), along with the two factor group components of A_g (green) and F_g (yellow) symmetry; the insets show the peaks of the A_g and F_g components to Ω_- from experiment[40] and theory. D) Atomic structure of the CO_2 molecule and crystal (cubic phase, $Pa\bar{3}$). E) Schematic representation of the two-phonon (top) and three-phonon (bottom) processes involved in the FR of solid CO_2. The plots of the spectra are produced with a developmental version of the CRYSTALpytools Python interface to CRYSTAL.[45] Peaks are modelled in terms of pseudo-Voigt profiles with 80% Lorentzian character (with half width at half maximum, HWHM, of 3 cm^{-1}, reduced to 0.03 cm^{-1} for the insets in panel C) and 20% Gaussian character (with standard deviation of 3 cm^{-1}). All spectra are simulated at 0 K.

bic phase with space group $Pa\bar{3}$, with four molecules per cell. Reciprocal space is sampled according to a 6×6×6 Monkhorst-Pack mesh, which corresponds to 24 **k** points in the symmetry-irreducible portion of the first Brillouin zone. Convergence of the self-consistent field process is controlled by a threshold on the energy set to a tight 10^{-9} Ha. A triple-zeta quality basis set is used (namely, pob-TZVP-rev2), which was specifically optimized for solid-state applications.[47] Energy and forces are computed with the B3LYP-D3 global hybrid exchange-correlation functional corrected for missing dispersive interactions,[48,49] which yields an optimized lattice parameter of 5.47 Å, with an experimentally extrapolated 0 K value of 5.54 Å.[50] The PES is described within 2M4T and 3M4T representations by use of EGH finite difference approaches.[17] Anharmonic vibrational states are computed through the VSCF and VCI methods.

The simulated Raman spectrum of solid CO_2 is shown in Figure 1 B) and C). As expected, a single peak is observed from the harmonic approximation (black solid line). The simulated spectrum obtained from the VSCF anharmonic method is reported as a grey solid line and still exhibits a single peak (red shifted by 17 cm^{-1}), which shows that a purely mean-field treatment of phonon couplings fails at describing the FR. By use of the VCI method, we are able to describe the Fermi dyad, with one important point to be addressed. Dashed and solid blue lines in Figure 1 B) and C) show the simulated VCI spectrum in the FR region as obtained from a 2M4T and 3M4T PES, respectively. Use of a 2M4T force field (neglecting three-phonon couplings, as done in previous studies[43,44]) only allows to take into account one of the two fundamental processes involved in the FR of the solid – the "molecular" one where the fundamental of an A_g stretching couples to the overtone of a bending, as in the top panel of Figure 1 E). Crucially, in terms of the

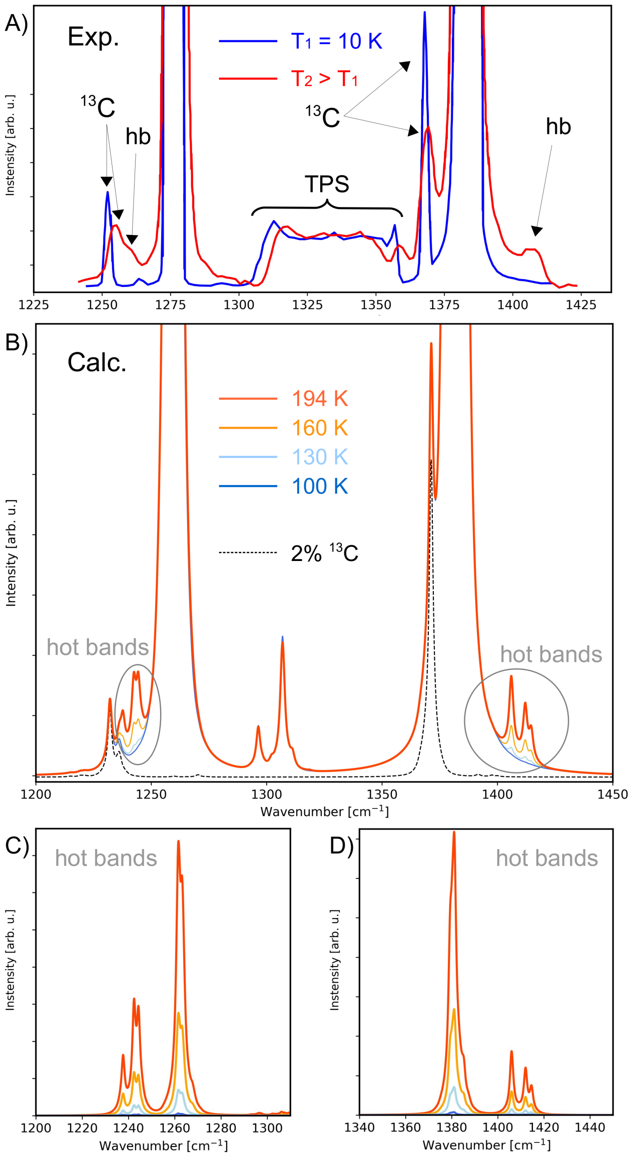

FIG. 2: Hot bands (hb) in the region of the Raman spectrum of solid CO$_2$. A) Experimental spectra recorded at 10 K (blue solid line)[27] and at higher temperature (red solid line)[31]; B) Simulated spectra at four temperatures (194, 160, 130 and 100 K). A 2% isotopic substitution of ^{13}C for ^{12}C has been modelled; C-D) Isolated contributions to the spectra of hot bands at different temperatures in the Ω_- and Ω_+ regions, respectively. In the simulated spectra, peaks are modelled as in Figure 1 with HWHM = 1.0 and 0.8 cm^{-1} for panels B) and C-D), respectively.

Raman spectrum, this results in the occurrence of three peaks: the two of the Fermi dyad and a residual peak of F_g character basically at the VSCF position. The intensity ratio I_+/I_- of the two peaks of the dyad is 1.78 in this case. Use of a 3M4T force field instead allows to take into account both fundamental processes involved in the FR of the solid including the three-phonon one of the bottom panel of Figure 1 E). This produces the solid blue spectrum in Figure 1 C) with the clean description of the FR. Now, as expected from the experiments, only the two peaks Ω_- and Ω_+ of the dyad are present, with an intensity ratio I_+/I_- of 2.04 in excellent agreement with the value from low-pressure experiments of 2.15.[27] Thus, we note that the separation δ between the two peaks does not change much when passing from a 2M4T to a 3M4T PES, while the intensity ratio does. Figure 1 C) also shows the individual A_g (two-mode, green line) and F_g (three-mode, yellow line) components of the spectrum. The two factor group components have been resolved by high-resolution, polarized, Raman measurements on single-crystal dry ice at 6 K.[40] The following was observed: i) In Ω_-, the two components give rise to two distinct peaks separated by 0.37 cm^{-1} and with an intensity ratio $I_-^{A_g}/I_-^{F_g}$ of about 3. Our calculations slightly overestimate the energy separation between the two but provide a strikingly good agreement on the intensity ratio – also of about 3 – as shown in the two insets of Figure 1 C); ii) In Ω_+, the two components are centered at the same position and can not be energy resolved. However, they still can be identified separately from polarized measurements (indeed, while the A_g component is linked to α_{xx}, α_{yy} and α_{zz} components of the polarizability tensor, the F_g component is linked to off-diagonal elements) and an intensity ratio $I_+^{A_g}/I_+^{F_g}$ of about 4 is observed. In our calculations, the two peaks are also centered at about the same position and are characterized by an intensity ratio of about 4, again in excellent agreement with the experiment,[40] see Figure 1 C).

Let us now address one anharmonic feature of the FR spectrum of solid CO$_2$ that has been overlooked so far, that is "hot bands" (hb) – i.e. spectral features associated to transitions between two vibrationally excited states. In general, IR intensities and Raman activities $I_{i\to f}$ associated to a transition between an initial state Ψ_i (with energy E_i) and a final state Ψ_f, as defined by our working expressions in Eqs. (3-11), also depend on temperature T through the statistical probability $p_i(T)$ of the initial state to be thermally populated:

$$I_{i\to f}(T) = I_{i\to f} \times p_i(T) \,, \tag{12}$$

where

$$p_i(T) = \frac{1}{Z} e^{-\frac{E_i}{k_B T}} \quad \text{with} \quad Z = \sum_{s}^{\text{all}} e^{-\frac{E_s}{k_B T}} \,. \tag{13}$$

We have implemented this correction, and here we take into account all those transitions that involve initial states with a Boltzmann population $p_i(T)$ larger than 0.01% at the selected temperature. Crucially, this allows us to determine the intensity of "hot bands". In particular, we show here that "hot bands" can manifest themselves as shoulders to the main peaks of the Fermi dyad, with an intensity that is of the same order of magnitude of that of shoulder peaks due to ^{12}C → ^{13}C isotopic substitution that were already identified and assigned.[27,31]

Figure 2 A) reports previous experimental Raman spectra recorded at different temperatures.[27,31] Two sharp shoulder peaks to the left of the two intense Fermi dyad ones are observed that were assigned to the isotopic substitution. Additional features are observed in the spectrum recorded at higher temperature (red line) that were not discussed and that we assign to "hot bands": a peak to the right of Ω_+ and a shoulder between the ^{13}C and ^{12}C Ω_- peaks. In Figure 2 B) we report our simulated spectra at four temperatures (194, 160, 130 and 100 K). The width of two-phonon state (TPS) continuum of bending modes is expectedly underestimated in our Γ point calculations as the full dispersion of bending phonons is not explicitly sampled. In all cases, a 2% isotopic substitution of ^{13}C for ^{12}C has been modelled (the contribution to the overall spectrum of ^{13}C fraction is shown as a black dashed line). The figure highlights two spectral regions with emerging features due to "hot bands". As expected, such features are very much temperature dependent and they almost disappear when T drops below 100 K. At temperatures larger than 130 K, they exhibit an intensity of the same order of magnitude of the 2% isotopic peaks, and nicely allow to explain the unassigned features in the high-temperature experimental spectrum of the top panel (red line). Figure 2 C-D) report the isolated contributions to the spectra from "hot bands" in the Ω_- and Ω_+ regions, respectively. It can be observed that, apart from the features already visible in Figure 2 B), "hot bands" also build intensity at the Ω_- and Ω_+ peaks. By inspection of the VCI states associated to such features, we can assign them to transitions between a singly excited bending mode as initial state Ψ_i and final states Ψ_f with leading configurations involving either one quantum of excitation on a stretching and one on a bending, or three quanta of excitation distributed among one, two, or three bendings.

In conclusion, we have presented an advanced computational methodology for the first-principles simulation of a variety of anharmonic features of infrared and Raman spectra of materials. Its application to the Fermi resonance of dry ice has allowed to showcase the accuracy of the approach and to characterize many subtle aspects of such anharmonic feature at the quantum-mechanical level for the first time.

Acknowledgments

This research has received funding from the Project CH4.0 under the MUR program "Dipartimenti di Eccellenza 2023-2027" (CUP: D13C22003520001).

---

[*] Electronic address: `alessandro.erba@unito.it`

[1] Larkin, P. *Infrared and Raman spectroscopy: principles and spectral interpretation*; Elsevier, 2017.

[2] Weber, W. H.; Merlin, R. *Raman scattering in materials science*; Springer Science & Business Media, 2000; Vol. 42.

[3] Suetaka, W.; Yates, J. T. *Surface infrared and Raman spectroscopy: methods and applications*; Springer Science & Business Media, 1995; Vol. 3.

[4] Jansen, T. L. Computational spectroscopy of complex systems. *J. Chem. Phys.* **2021**, *155*.

[5] Grunenberg, J. *Computational spectroscopy: methods, experiments and applications*; John Wiley & Sons, 2011.

[6] Barone, V.; Alessandrini, S.; Biczysko, M.; Cheeseman, J. R.; Clary, D. C.; McCoy, A. B.; DiRisio, R. J.; Neese, F.; Melosso, M.; Puzzarini, C. Computational molecular spectroscopy. *Nat. Rev. Methods Primers* **2021**, *1*, 38.

[7] Sinha, P.; Boesch, S. E.; Gu, C.; Wheeler, R. A.; Wilson, A. K. Harmonic vibrational frequencies: scaling factors for HF, B3LYP, and MP2 methods in combination with correlation consistent basis sets. *J. Phys. Chem. A* **2004**, *108*, 9213–9217.

[8] Andersson, M. P.; Uvdal, P. New scale factors for harmonic vibrational frequencies using the B3LYP density functional method with the triple-ζ basis set 6-311+ G (d, p). *J. Phys. Chem. A* **2005**, *109*, 2937–2941.

[9] Alecu, I.; Zheng, J.; Zhao, Y.; Truhlar, D. G. Computational thermochemistry: scale factor databases and scale factors for vibrational frequencies obtained from electronic model chemistries. *J. Chem. Theory Comput.* **2010**, *6*, 2872–2887.

[10] Katsyuba, S. A.; Zvereva, E. E.; Burganov, T. I. Is there a simple way to reliable simulations of infrared spectra of organic compounds? *J. Phys. Chem. A* **2013**, *117*, 6664–6670.

[11] Fábri, C.; Szidarovszky, T.; Magyarfalvi, G.; Tarczay, G. Gas-phase and Ar-matrix SQM scaling factors for various DFT functionals with basis sets including polarization and diffuse functions. *J. Phys. Chem. A* **2011**, *115*, 4640–4649.

[12] Barone, V.; Biczysko, M.; Bloino, J. Fully anharmonic IR and Raman spectra of medium-size molecular systems: accuracy and interpretation. *Phys. Chem. Chem. Phys.* **2014**, *16*, 1759–1787.

[13] Franke, P. R.; Stanton, J. F.; Douberly, G. E. How to VPT2: accurate and intuitive simulations of CH stretching infrared spectra using VPT2+ K with large effective Hamiltonian resonance treatments. *J. Phys. Chem. A* **2021**, *125*, 1301–1324.

[14] Nyquist, R. A. *Interpreting infrared, Raman, and nuclear magnetic resonance spectra*; Academic Press, 2001; Vol. 2.

[15] Markland, T. E.; Ceriotti, M. Nuclear quantum effects enter the mainstream. *Nat. Rev. Chem.* **2018**, *2*, 0109.

[16] Basire, M.; Mouhat, F.; Fraux, G.; Bordage, A.; Hazemann, J.-L.; Louvel, M.; Spezia, R.; Bonella, S.; Vuilleumier, R. Fermi resonance in CO_2: Mode assignment and quantum nuclear effects from first principles molecular dynamics. *J. Chem. Phys.* **2017**, *146*, 134102.

[17] Erba, A.; Maul, J.; Ferrabone, M.; Carbonniére, P.; Rérat, M.; Dovesi, R. Anharmonic Vibrational States of Solids from DFT Calculations. Part I: Description of the

Potential Energy Surface. *J. Chem. Theory Comput.* **2019**, *15*, 3755–3765.

[18] Erba, A.; Maul, J.; Ferrabone, M.; Dovesi, R.; Rérat, M.; Carbonnière, P. Anharmonic Vibrational States of Solids from DFT Calculations. Part II: Implementation of the VSCF and VCI Methods. *J. Chem. Theor. Comput.* **2019**, *15*, 3766–3777.

[19] CarbonnieÃÄre, P.; Erba, A.; Richter, F.; Dovesi, R.; Rérat, M. Calculation of anharmonic IR and Raman intensities for periodic systems from DFT calculations: Implementation and validation. *J. Chem. Theory Comput.* **2020**, *16*, 3343–3351.

[20] Mitoli, D.; Maul, J.; Erba, A. Anharmonic Terms of the Potential Energy Surface: A Group Theoretical Approach. *Crystal Growth & Design* **2023**, *23*, 3671–3680.

[21] Erba, A.; Desmarais, J. K.; Casassa, S.; Civalleri, B.; Doná, L.; Bush, I. J.; Searle, B.; Maschio, L.; Edith-Daga, L.; Cossard, A.; Ribaldone, C.; Ascrizzi, E.; Marana, N. L.; Flament, J.-P.; Kirtman, B. CRYSTAL23: A Program for Computational Solid State Physics and Chemistry. *J. Chem. Theor. Comput.* **2023**, *19*, 6891–6932.

[22] Maul, J.; Spoto, G.; Mino, L.; Erba, A. Elucidating the structure and dynamics of CO ad-layers on MgO surfaces. *Phys. Chem. Chem. Phys.* **2019**, *21*, 26279–26283.

[23] Schireman, R. G.; Maul, J.; Erba, A.; Ruggiero, M. T. Anharmonic Coupling of Stretching Vibrations in Ice: A Periodic VSCF and VCI Description. *J. Chem. Theory Comput.* **2022**, *18*, 4428–4437.

[24] Maschio, L.; Kirtman, B.; Orlando, R.; Rèrat, M. Ab initio analytical infrared intensities for periodic systems through a coupled perturbed Hartree-Fock/Kohn-Sham method. *J. Chem. Phys.* **2012**, *137*.

[25] Dovesi, R.; Kirtman, B.; Maschio, L.; Maul, J.; Pascale, F.; Rérat, M. Calculation of the infrared intensity of crystalline systems. A comparison of three strategies based on berry phase, wannier function, and coupled-perturbed Kohn–Sham methods. *J. Phys. Chem. C* **2018**, *123*, 8336–8346.

[26] Maschio, L.; Kirtman, B.; Rérat, M.; Orlando, R.; Dovesi, R. Ab initio analytical Raman intensities for periodic systems through a coupled perturbed Hartree-Fock/Kohn-Sham method in an atomic orbital basis. I. Theory. *J. Chem. Phys.* **2013**, *139*.

[27] Bogani, F.; Salvi, P. R. Fermi resonance in solid CO_2. *J. Chem. Phys.* **1984**, *81*, 4991–5001.

[28] Cardini, G.; Remigio Salvi, P.; Schettino, V.; Jodl, H. J. Pressure tuning of Fermi resonance in crystal CO_2. *J. Chem. Phys.* **1989**, *91*, 3869–3876.

[29] Schrader, B.; Moore, D. Laser-based molecular spectroscopy for chemical analysis-Raman scattering processes. *Pure Appl. Chem.* **1997**, *69*, 1451–1468.

[30] Bier, K.; Jodl, H. Tuning of the Fermi resonance of CO_2 and CS_2 by temperature, pressure, and matrix material. *J. Chem. Phys.* **1987**, *86*, 4406–4410.

[31] Nosenko, V. V.; Rudko, G. Y.; Yaremko, A. M.; Yukhymchuk, V. O.; Hreshchuk, O. M. Anharmonicity and Fermi resonance in the vibrational spectra of a CO_2 molecule and CO_2 molecular crystal: Similarity and distinctions. *J. Raman Spectrosc.* **2018**, *49*, 559–568.

[32] Fermi, E. Über den ramaneffekt des kohlendioxyds. *Z. Phys.* **1931**, *71*, 250–259.

[33] Li, L.; Du, Z.; Zhang, X.; Xi, S.; Wang, B.; Luan, Z.; Lian, C.; Yan, J. In situ Raman spectral characteristics of carbon dioxide in a deep-sea simulator of extreme environments reaching 300ÑÉ and 30 MPa. *Appl. Spectrosc.* **2018**, *72*, 48–59.

[34] Osberg, W.; Hornig, D. The vibrational spectra of molecules and complex ions in crystals. VI. Carbon dioxide. *J. Chem. Phys.* **1952**, *20*, 1345–1347.

[35] Cahill, J.; Leroi, G. Raman spectra of solid CO_2, N_2O, N_2, and CO. *J. Chem. Phys.* **1969**, *51*, 1324–1332.

[36] Hanson, R.; Jones, L. Infrared and Raman studies of pressure effects on the vibrational modes of solid CO_2. *J. Chem. Phys.* **1981**, *75*, 1102–1112.

[37] Ranson, P.; Ouillon, R.; Califano, S. High-resolution Raman investigation of the vibrational relaxation of two-phonon bound states in solid CO_2 at different temperatures. *J. Raman Spectrosc.* **1986**, *17*, 155–159.

[38] Olijnyk, H.; Däufer, H.; Jodl, H.-J.; Hochheimer, H. Effect of pressure and temperature on the Raman spectra of solid CO_2. *J. Chem. Phys.* **1988**, *88*, 4204–4212.

[39] Bogani, F. Two-phonon resonances and bound-states in molecular crystals. I. General theory. *J. Phys. C: Solid State Phys.* **1978**, *11*, 1283.

[40] Ouillon, R.; Ranson, P.; Califano, S. High resolution Raman spectra of the Fermi diad in crystalline CO_2 at 6 K. *J. Chem. Phys.* **1985**, *83*, 2162–2164.

[41] Cardini, G.; Schettino, V. Comment on "Fermi resonance in solid CO_2 under pressure" [J. Chem. Phys. 138, 074501 (2013)]. *J. Chem. Phys.* **2014**, *140*, 177101.

[42] Rodriguez-Garcia, V.; Hirata, S.; Yagi, K.; Hirao, K.; Taketsugu, T.; Schweigert, I.; Tasumi, M. Fermi resonance in CO_2: A combined electronic coupled-cluster and vibrational configuration-interaction prediction. *J. Chem. Phys.* **2007**, *126*, 124303.

[43] Sode, O.; Keçeli, M.; Yagi, K.; Hirata, S. Fermi resonance in solid CO_2 under pressure. *J. Chem. Phys.* **2013**, *138*, 074501.

[44] Hirata, S.; Sode, O.; Keçeli, M.; Yagi, K.; Li, J. Response to "Comment on 'Fermi resonance in solid CO_2 under pressure'" [J. Chem. Phys. 140, 177101 (2014)]. *J. Chem. Phys.* **2014**, *140*, 177101.

[45] Camino, B.; Zhou, H.; Ascrizzi, E.; Boccuni, A.; Bodo, F.; Cossard, A.; Mitoli, D.; Ferrari, A. M.; Erba, A.; Harrison, N. M. CRYSTALpytools: a Python Infrastructure for the CRYSTAL Code. *Comput. Phys. Commun.* **2023**, *292*, 108853.

[46] Erba, A.; Baima, J.; Bush, I.; Orlando, R.; Dovesi, R. Large Scale Condensed Matter DFT Simulations: Performance and Capabilities of the CRYSTAL Code. *J. Chem. Theory Comput.* **2017**, *13*, 5019–5027.

[47] Vilela Oliveira, D.; Laun, J.; Peintinger, M. F.; Bredow, T. BSSE-correction scheme for consistent gaussian basis sets of double-and triple-zeta valence with polarization quality for solid-state calculations. *J. Comput. Chem.* **2019**, *40*, 2364–2376.

[48] Becke, A. D. Density-functional thermochemistry. III. The role of exact exchange. *J. Chem. Phys.* **1993**, *98*, 5648.

[49] Grimme, S.; Antony, J.; Ehrlich, S.; Krieg, H. A consistent and accurate ab initio parametrization of density functional dispersion correction (DFT-D) for the 94 elements H-Pu. *J. Chem. Phys.* **2010**, *132*, 154104.

[50] Keesom, W.; KàöàÇhler, J. The lattice constant and expansion coefficient of solid carbon dioxide. *Physica* **1934**, *1*, 655–658.